Hindawi
Applied Bionics and Biomechanics
Volume 2022, Article ID 8550869, 15 pages
https://doi.org/10.1155/2022/8550869

Research Article

Design and Investigation of an Asymmetric Logarithmic Spiral Gear Drive

Zenghuang He,[1] **Xu Gong**,[1] **Shengping Fu**,[1] **Shanming Luo**,[1] **and Jingyu Mo**[1,2]

[1]*College of Marine Equipment and Mechanical Engineering, Jimei University, Xiamen 361021, China*
[2]*School of Aerospace Engineering, Xiamen University, Xiamen 361005, China*

Correspondence should be addressed to Xu Gong; 373632159@qq.com and Shengping Fu; 7025370@163.com

Received 12 May 2022; Revised 29 July 2022; Accepted 26 October 2022; Published 26 December 2022

Academic Editor: Guowu Wei

Sliding on gear teeth working surfaces has negative effects on the performances of gears, such as tooth surface wear, pitting, etc. In order to reduce the gear sliding during high speed and heavy load, a new type of pure rolling gear, named as an asymmetric logarithmic spiral gear, is designed referring to the characteristics of the *Issus* planthopper gear. To explore the meshing principle of this kind of gear, the equations of the teeth surfaces, their working lines, and contact lines are all derived. Then, the tooth profile parameters and slip rate are calculated. To ensure accurate gear engagement, the gear interferences are analyzed to build the gear models. Subsequently, the gear is performed to simulate its working condition by the finite element method. Furthermore, the results are compared with that of the pure rolling single arc gear. As a result, the asymmetric logarithmic spiral gear behaviors less contact and bending stresses than the pure rolling single arc gear under the same work condition.

1. Introduction

Gear has the advantages of compact structure, smooth transmission, and constant transmission ratio, so it is widely used in various fields. When most gears transmit power, rolling and sliding occur simultaneously on the working surfaces of the gear teeth. Sliding may cause wear, gluing, and plastic deformation. Especially under the condition of high speed and heavy load, it reduces the transmission efficiency, increases the energy consumption, shortens the life of gear, and produces the larger vibration and noise. The lubricants are usually used to mitigate these problems, leading to food contamination in the food machinery industry.

In order to reduce the slip between gear teeth surfaces, scholars have done a lot of explorations and researches on pure rolling gears. Tan et al. [1] derived a simplified equation for the bevel gear to satisfy continuous pure rolling contact. Chen et al. [2–4] introduced the geometric design, meshing performance, and mechanical property of a new pure rolling gear. Xiao et al. [5] designed a pure rolling noncircular gear with fewer teeth. He et al. [6] proposed a pure rolling gear with divisible center distance. Wagner et al. [7] proposed the gear profiles of pure rolling contact for parallel axis transmission. Tao et al. [8] studied the meshing principle and characteristics of a new type of bihemispheric rolling gear and applied it to engineering. Song et al. [9] proposed a new pure rolling cycloid gear and applied it to the reducer, which could achieve higher transmission efficiency. Xue et al. [10] proposed a new cycloid gear transmission, which could realize pure rolling and improve the contact ratio and the service life. Tan et al. [11] studied the geometric principle and processing process of the pure rolling cycloidal gear and completed the performance experiment. X. Huang and A. Huang [12] established the constraint conditions of the pure rolling contact gear and found a variety of simple and practical tooth profile curves of pure rolling gear. Chen et al. [13] designed a new type of pure circular arc rolling helical gear and made a prototype for test. It was concluded that this kind of gear has pure rolling contact, high coincidence ratio, and large comprehensive strength. Geng, Zhou, and Zhao [14–16] studied the theory and performance of pure rolling single arc gear. Based on the conjugate curve method, Liang et al. [17–20] proposed a circular arc gear with a sliding rate close to zero, which is approximate to pure rolling contact.

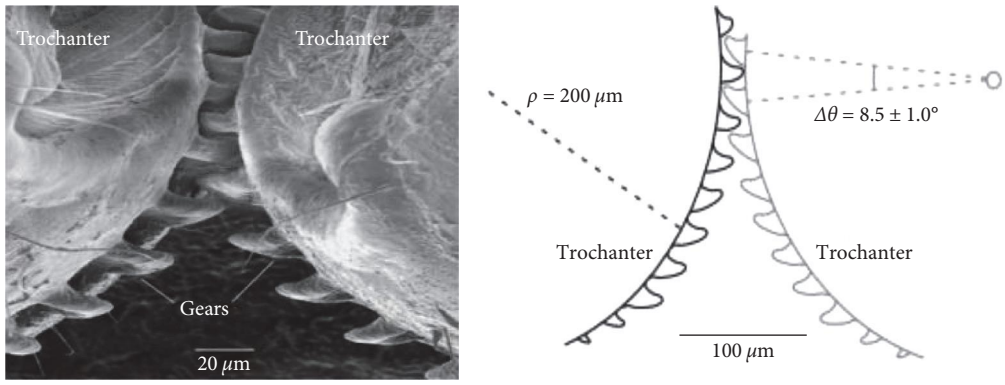

Figure 1: Natural gear of the *Issus* planthopper [21].

To sum up, pure rolling theory has been applied to several kinds of gears, such as bevel gear, noncircular gear, cycloidal gear, and arc gear. The pure rolling bevel gear is mainly used in the occasion where two axes intersect. The pure rolling noncircular gear is mainly applied in the occasion of low speed and special periodic motion. The pure rolling constraint equations of these two gears are obtained by controlling the contact points velocity to zero. The pure rolling cycloid gear realizes pure rolling contact under the condition that the contact point is the velocity instantaneous center. It is mainly used in planetary mechanism of the reducer. The pure rolling single arc gear can realize pure rolling by limiting the contact points to the pitch line. It is mainly used in high speed and heavy load transmission with two parallel shafts. However, the machining of the pure rolling single circular arc gear requires two cutting tools, so its universality is poor.

Burrows and Sutton [21] found a pair of gears in the hip joint of the planthopper, as shown in Figure 1. The working characteristics of the *Issus* planthopper gear are high speed and heavy load. Referring to the tooth shape of the *Issus* planthopper gear and the shortcoming of the pure rolling single arc gear, a new pure rolling gear is proposed in this paper, which is designed to be used in high speed and heavy load transmission with parallel shafts.

As shown in Figure 2, the new gear tooth shape is asymmetrical with a convex tooth profile on one side and a concave tooth profile on the other side based on the shape of the *Issus* planthopper gear. Since the tooth profiles of the *Issus* planthopper gear are naturally generated and the logarithmic helix is also a natural curve, the tooth profiles of the *Issus* planthopper gear are assumed to be logarithmic helix. Wang [22] proved the feasibility of logarithmic helices as gear tooth profile. Therefore, the logarithmic helix is taken as the working tooth profiles of the new gear, which is named as an asymmetric logarithmic spiral gear.

The rest of this paper is organized as follows: Section 2 explores the gear meshing principle, including the equations of the tooth surface, working line, contact line, tooth profile parameters, and sliding ratio. Section 3 analyzes the gear interferences, including the geometric interference, root cutting,

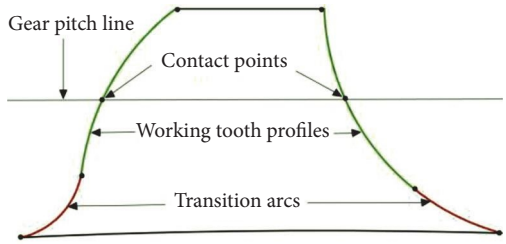

Figure 2: Tooth profile of the asymmetric logarithmic spiral gear.

and tooth profile overlapping interference. In Section 4, the gear models are built to ensure the accurate gear engagement and the gear stress distributions are simulated and analyzed.

2. Meshing Mechanism

The asymmetric logarithmic spiral gear is a kind of helical gear and can realize bidirectional transmission. To ensure the correct transmission, it is necessary to meet the contact ratio greater than or equal to 1, the pressure angles of the meshing teeth profiles are equal, and the helical angles of the driving and driven gears are equal in magnitude and opposite direction. Figure 3(a) shows the meshing teeth profiles. The four working teeth profiles are represented as C_1, C_2, C_3, and C_4, respectively. The teeth surfaces formed by the four teeth profiles are represented as Σ_1, Σ_2, Σ_3, and Σ_4, respectively, as shown in Figure 3(b). When the gear 1 rotates counterclockwise, Σ_1 and Σ_2 are the conjugate teeth surfaces. When the gear 1 rotates clockwise, Σ_3 and Σ_4 are the conjugate teeth surfaces.

2.1. Tooth Surface Equations. The formation of the tooth surface Σ_1 is taken as an example. The coordinate system is established, as shown in Figure 4 [23]. $S_1(O_1\text{-}x_1y_1z_1)$ is a moving coordinate fixedly connected with the gear 1. $S(O\text{-}xyz)$ is a fixed coordinate system of the gear 1 with z-axis parallel to z_1 axis. $S_{p1}(O_{p1}\text{-}x_{p1}y_{p1}z_{p1})$ is a coordinate system fixedly connected with the rack of the tooth profile C_1, x_{p1} axis is parallel to x-axis, and z_{p1} axis is parallel to z-axis. $S_{s1}(O_{s1}\text{-}x_{s1}y_{s1}z_{s1})$ is a coordinate system where the section of the tooth profile C_1 is located. o_1 is the center of

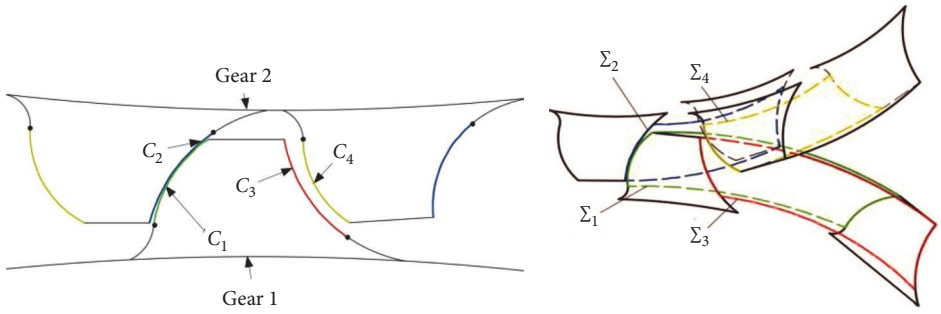

FIGURE 3: Introduction of the asymmetric logarithmic spiral gear tooth profile.

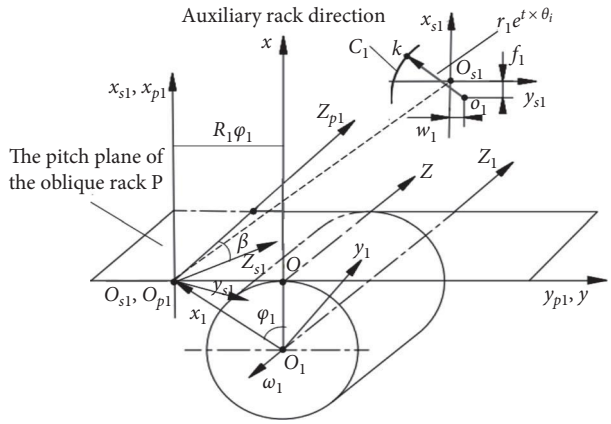

FIGURE 4: Schematic diagram of the gear 1 convex tooth surface formation.

the convex tooth profile. β is the spiral angle of the gear 1. R_1 is the radius of the pitch cylinder of the gear 1. φ_1 is the gear 1 rotation angle. ω_1 is the gear 1 angular rotational velocity. Suppose P is a helical rack, and its convex tooth surface Σ_{P1} is formed by scanning along the z_{s1} axis using the tooth profile C_1. The pitch plane of the helical rack P is tangent to the gear 1 pitch cylinder.

When the gear 1 rotates clockwise at an angular velocity of ω_1, the pitch plane of the helical rack P is shifted along the y-axis at the speed of $\omega_1 R_1$. In this generating motion, the tooth surface Σ_1 is formed by the tooth surface Σ_{P1}.

The convex tooth profile C_1 equation in the coordinate system:

$$\begin{aligned} x_{s1}(\theta) &= a_1 - f_1, \\ y_{s1}(\theta) &= -(b_1 - w_1), \\ z_{s1}(\theta) &= 0, \end{aligned} \tag{1}$$

where $a_1 = r_1 e^{t\times\theta_{i1}} \sin\theta_{i1}$, r_1 is the initial circle radius of the convex tooth profile C_1, t is the logarithmic helical coefficient, θ_{i1} is the angle of any point on the tooth profile C_1, $b_1 = r_1 e^{t\times\theta_{i1}} \cos\theta_{i1}$, f_1 and w_1 are the offset distance of the tooth profile C_1 center point o_1 relative to the x_{s1} and y_{s1} axes, respectively.

Based on the coordinate transformation principle, Equation (1) is transformed from the coordinate system $S_{s1}(O_{s1}\text{-}x_{s1}y_{s1}z_{s1})$ to the coordinate system $S_{p1}(O_{p1}\text{-}x_{p1}y_{p1}z_{p1})$. The transformation matrix equation is expressed as follows:

$$\begin{bmatrix} x_{p1} \\ y_{p1} \\ z_{p1} \\ 1 \end{bmatrix} = \begin{bmatrix} 1 & 0 & 0 & 0 \\ 0 & \cos\beta & \sin\beta & \mu\sin\beta \\ 0 & -\sin\beta & \cos\beta & \mu\cos\beta \\ 1 & 0 & 0 & 0 \end{bmatrix} \begin{bmatrix} x_{s1} \\ y_{s1} \\ z_{s1} \\ 1 \end{bmatrix}. \tag{2}$$

The equation of the tooth profile C_1 in the coordinate system $S_{p1}(O_{p1}\text{-}x_{p1}y_{p1}z_{p1})$ can be obtained.

$$\begin{aligned} x_{p1} &= a_1 - f_1, \\ y_{p1} &= -(b_1 - w_1)\cos\beta + \mu_1 \sin\beta, \\ z_{p1} &= (b_1 - w_1)\sin\beta + \mu_1 \cos\beta. \end{aligned} \tag{3}$$

The expression of the contact condition can be derived by using the instantaneous rotation axis method [23].

$$\begin{aligned} &[(b_1 - w_1)\cos\beta - \mu_1 \sin\beta + R_1\varphi_1] \cdot (-tb_1 + a_1) \\ &+(a_1 - f_1)(ta_1 + b_1)\cos\beta = 0. \end{aligned} \tag{4}$$

Equation (3) is transformed into the coordinate system $S_1(O_1\text{-}x_1y_1z_1)$; then, the result is combined with Equation (4) to obtain the convex tooth surface Σ_1 equation.

$$\begin{aligned} x_1 &= (a_1 - f_1 + R_1)\cos\varphi_1 - \frac{(a_1 - f_1)(ta_1 + b_1)\cos\beta}{tb_1 - a_1}\sin\varphi_1, \\ y_1 &= (a_1 - f_1 + R_1)\sin\varphi_1 + \frac{(a_1 - f_1)(ta_1 + b_1)\cos\beta}{tb_1 - a_1}\cos\varphi_1, \\ z_1 &= (b_1 - w_1)\sin\beta + \cot\beta\left[\frac{(a_1 - f_1)(ta_1 + b_1)\cos\beta}{tb_1 - a_1}\right. \\ &\quad \left. + (b_1 - w_1)\cos\beta + R_1\varphi_1\right]. \end{aligned} \tag{5}$$

The coordinate systems in Figure 5 are established to derive the concave tooth surface Σ_2 equation. $S(O\text{-}xyz)$ is a fixed coordinate system of the gear 2 with z-axis parallel

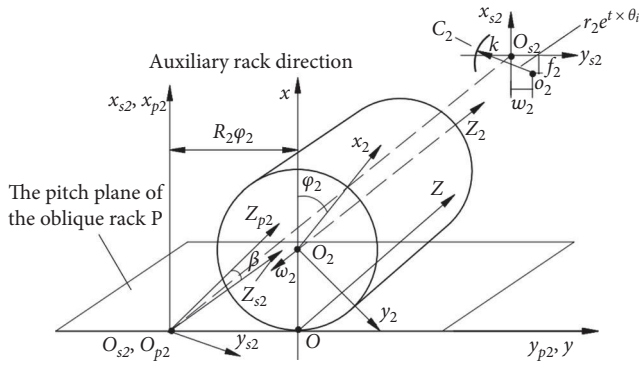

Figure 5: Schematic diagram of the gear 2 concave tooth surface formation.

to z_2 axis. The subscript of the expression symbol in Figure 5 is changed from 1 to 2.

The concave tooth profile C_2 equation in the coordinate system $S_{s2}(O_{s2}\text{-}x_{s2}y_{s2}z_{s2})$ is obtained as follows:

$$\begin{aligned} x_{s2}(\theta) &= a_2 - f_2, \\ y_{s2}(\theta) &= -b_2 + w_2, \\ z_{s2}(\theta) &= 0, \end{aligned} \tag{6}$$

where $a_2 = r_2e^{t\times\theta_{i2}}\sin\theta_{i2}$, r_2 is the initial circle radius of the concave tooth profile C_2, θ_{i2} is the angle of any point on the tooth profile C_2, $b_2 = r_2e^{t\times\theta_{i2}}\cos\theta_{i2}$, f_2 and w_2 are the offset distance of the tooth profile C_2 center point o_2 relative to the x_{s2} and y_{s2} axes, respectively.

Similarly, the tooth surface Σ_2 equation can be obtained as follows:

$$\begin{aligned} x_2 &= (a_2 - f_2 - R_2)\cos\varphi_2 + \frac{(a_2 - f_2)(ta_2 + b_2)\cos\beta}{tb_2 - a_2}\sin\varphi_2, \\ y_2 &= -(a_2 - f_2 - R_2)\sin\varphi_2 + \frac{(a_2 - f_2)(ta_2 + b_2)\cos\beta}{tb_2 - a_2}\cos\varphi_2, \\ z_2 &= (b_2 - w_2)\sin\beta + \cot\beta\left[\frac{(a_2 - f_2)(ta_2 + b_2)\cos\beta}{tb_2 - a_2}\right. \\ &\quad \left. + (b_2 - w_2)\cos\beta + R_2\varphi_2\right]. \end{aligned} \tag{7}$$

As shown in Figure 6, the tooth profile C_3 can be obtained by transforming the position of the tooth profile C_2 in the coordinate system $S_s(O_s\text{-}x_sy_sz_s)$. The tooth profile C_2 is symmetric along the y_s axis and then is moved to the tooth profile C_3 with distances of c and d along the x_s and y_s axes, respectively. The contact points of the tooth profiles C_2 and C_3 are k_1 and k_2, respectively. The line $\overline{k_1k_2}$ intersects x_s axis at point p. The length of $\overline{k_1p}$ is the same as the length of $\overline{k_2p}$.

The equation of the concave tooth profile C_3 in the coordinate system $S_s(O_s\text{-}x_sy_sz_s)$ can be obtained as follows:

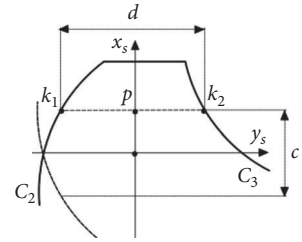

Figure 6: Coordinate transformation of concave tooth profile.

$$\begin{aligned} x_{s1}(\theta) &= -(a_2 - f_2) + c, \\ y_{s1}(\theta) &= -b_2 + w_2 + d, \\ z_{s1}(\theta) &= 0, \end{aligned} \tag{8}$$

where $c = 2(r_1e^{t\times\theta_0}\sin\theta_0 - f_1)$, $d = 2(r_1e^{t\times\theta_0}\cos\theta_0 - w_1)$.

The tooth surface Σ_3 equation can be obtained by referring to the formation of the tooth surface Σ_1.

$$\begin{aligned} x_3 &= (-a_2 + f_2 + c + R_1)\cos\varphi_1 \\ &\quad - \frac{(-a_2 + f_2 + c)(ta_2 + b_2)\cos\beta}{tb_2 - a_2}\sin\varphi_1, \\ y_3 &= (-a_2 + f_2 + c + R_1)\sin\varphi_1 \\ &\quad + \frac{(-a_2 + f_2 + c)(ta_2 + b_2)\cos\beta}{tb_2 - a_2}\cos\varphi_1, \\ z_3 &= (b_2 - w_2 + d)\sin\beta \\ &\quad + \cot\beta\left[\frac{(-a_2 + f_2 + c)(ta_1 + b_1)\cos\beta}{tb_1 - a_1}\right. \\ &\quad \left. + (b_2 - w_2 + d)\cos\beta + R_1\varphi_1\right]. \end{aligned} \tag{9}$$

Similarly, the tooth surface Σ_4 equation can be obtained by referring to the formation of the tooth surface Σ_2.

$$\begin{aligned} x_4 &= (-a_1 + f_1 + c - R_2)\cos\varphi_2 \\ &\quad + \frac{(-a_1 + f_1 + c)(ta_1 + b_1)\cos\beta}{tb_1 - a_1}\sin\varphi_2, \\ y_4 &= -(-a_1 + f_1 + c - R_2)\sin\varphi_2 \\ &\quad + \frac{(-a_1 + f_1 + c)(ta_1 + b_1)\cos\beta}{tb_1 - a_1}\cos\varphi_2, \\ z_4 &= (b_1 - w_1 + d)\sin\beta + \cot\beta\left[\frac{(a_1 - f_1 + c)(ta_1 + b_1)\cos\beta}{tb_1 - a_1}\right. \\ &\quad \left. + (b_1 - w_1 + d)\cos\beta + R_2\varphi_2\right]. \end{aligned} \tag{10}$$

2.2. Contact Line and Tooth Surface Working Line. The contact line of the asymmetric logarithmic spiral gear is the trajectory of the instantaneous contact points in the fixed coordinate system $S(O\text{-}xyz)$. The tooth surface working line is the collection of the theoretical contact points on the teeth surfaces in the transmission process. By deducing the equations of the contact line and tooth surface working line, the pure rolling conditions can be obtained.

The tooth surface Σ_1 meshing with the tooth surface Σ_2 is taken as an example. As shown in Figure 4, the tooth profile C_1 in the coordinate system $S_{p1}(O_{p1}\text{-}x_{p1}y_{p1}z_{p1})$ is moved to the coordinate system $S(O\text{-}xyz)$ with a distance of $R_1\varphi_1$ along the y-axis. Then, Equation (4) can be used to obtain the meshing surface equation. In the meshing surface equation, when $\theta_i = \theta_0$, the equation of the contact line of the tooth surface Σ_1 can be obtained as follows:

$$\begin{aligned} x_{m1} &= a_0 - f_1, \\ y_{m1} &= \frac{(a_0 - f_1)(ta_0 + b_0)\cos\beta}{tb_0 - a_0}, \\ z_{m1} &= (b_0 - w_1)\sin\beta + \cot\beta\left[\frac{(a_0 - f_1)(ta_0 + b_0)\cos\beta}{tb_0 - a_0}\right. \\ &\quad \left. + (b_0 - w_1)\cos\beta + R_1\varphi_1\right], \end{aligned} \tag{11}$$

where $a_0 = r_1 e^{t\times\theta_0}\sin\theta_0, b_0 = r_1 e^{t\times\theta_0}\cos\theta_0$.

Similarly, the equation of the contact line of the surface Σ_2 can be obtained.

$$\begin{aligned} x_{m2} &= a_3 - f_2, \\ y_{m2} &= \frac{(a_3 - f_2)(ta_3 + b_3)\cos\beta}{tb_3 - a_3}, \\ z_{m2} &= (b_3 - w_3)\sin\beta + \cot\beta\left[\frac{(a_3 - f_2)(ta_3 + b_3)\cos\beta}{tb_3 - a_3}\right. \\ &\quad \left. + (b_3 - w_2)\cos\beta + R_2\varphi_2\right], \end{aligned} \tag{12}$$

where $a_3 = r_2 e^{t\times\theta_0}\sin\theta_0$, $b_3 = r_2 e^{t\times\theta_0}\cos\theta_0$.

In Equation (5), when $\theta_i = \theta_0$, the equation of the tooth surface working line of the tooth surface Σ_1 is obtained as follows:

$$\begin{aligned} x_{w1} &= (a_0 - f_1 + R_1)\cos\varphi_1 - \frac{(a_0 - f_1)(ta_0 + b_0)\cos\beta}{tb_0 - a_0}\sin\varphi_1, \\ y_{w1} &= (a_0 - f_1 + R_1)\sin\varphi_1 + \frac{(a_0 - f_1)(ta_0 + b_0)\cos\beta}{tb_0 - a_0}\cos\varphi_1, \\ z_{w1} &= (b_0 - w_1)\sin\beta + \cot\beta\left[\frac{(a_0 - f_1)(ta_0 + b_0)\cos\beta}{tb_0 - a_0}\right. \\ &\quad \left. + (b_0 - w_1)\cos\beta + R_1\varphi_1\right]. \end{aligned} \tag{13}$$

In Equation (7), when $\theta_i = \theta_0$, the equation of the tooth surface working line of the tooth surface Σ_2 is obtained as follows:

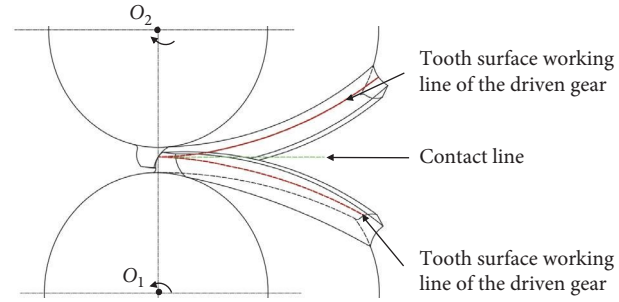

FIGURE 7: Schematic diagram of the contact line and tooth surface working line.

$$\begin{aligned} x_{w2} &= (a_3 - f_2 - R_2)\cos\varphi_2 + \frac{(a_3 - f_2)(ta_3 + b_3)\cos\beta}{tb_2 - a_2}\sin\varphi_2, \\ y_{w2} &= -(a_3 - f_2 - R_2)\sin\varphi_2 + \frac{(a_3 - f_2)(ta_3 + b_3)\cos\beta}{tb_3 - a_3}\cos\varphi_2, \\ z_{w2} &= (b_3 - w_2)\sin\beta + \cot\beta\left[\frac{(a_3 - f_2)(ta_3 + b_3)\cos\beta}{tb_3 - a_3}\right. \\ &\quad \left. + (b_3 - w_2)\cos\beta + R_2\varphi_2\right]. \end{aligned} \tag{14}$$

According to the characteristics of the pure rolling point contact [14], the contact points are limited to the nodal line, which means that the distances between the contact lines and the nodal line are zero, that is, $l = \sqrt{x^2 + y^2} = 0$. By combining Equations (11) and (12), the pure rolling constraint equations can be obtained as follows:

$$\begin{aligned} f_1 &= r_1 e^{t\times\theta_0}\sin\theta_0, \\ f_2 &= r_2 e^{t\times\theta_0}\sin\theta_0. \end{aligned} \tag{15}$$

Equation (15) is substituted into Equations (11)–(14). It can be known that the teeth surfaces working lines of the driving and driven gears are both helices on the teeth surfaces. The contact lines of the driving and driven gears are both straight lines parallel to the rotation axis of the gear pair, as shown in Figure 7.

2.3. Tooth Profile Parameters. Figures 8(a) and 8(b) show the meshing diagram of the tooth profiles C_1 and C_2. j is the side clearance of the gear. h_{g1} and h_{g2} are the vertical distances from the transition points k_a and k_b to the nodal line, respectively. h_a and h_f are the tooth addendum and dedendum, respectively. In the coordinate systems $S_{G1}(O_{G1}\text{-}x_{G1}y_{G1}z_{G1})$ and $S_{G2}(O_{G2}\text{-}x_{G2}y_{G2}z_{G2})$, O_{G1} is the center point of the gear tooth thickness, O_{G2} is the center point of the gear tooth groove width, and x_{G1} and x_{G2} coincide with the pitch lines of the gears 1 and 2, respectively. o_1 and o_2 are the center points of the convex and concave tooth profiles, respectively. θ_0 and θ_3 are the pressure angles of the convex and concave tooth profiles, respectively. θ_0 is equal to θ_3. θ_1 and θ_4 are the process angles of the convex and concave tooth profiles,

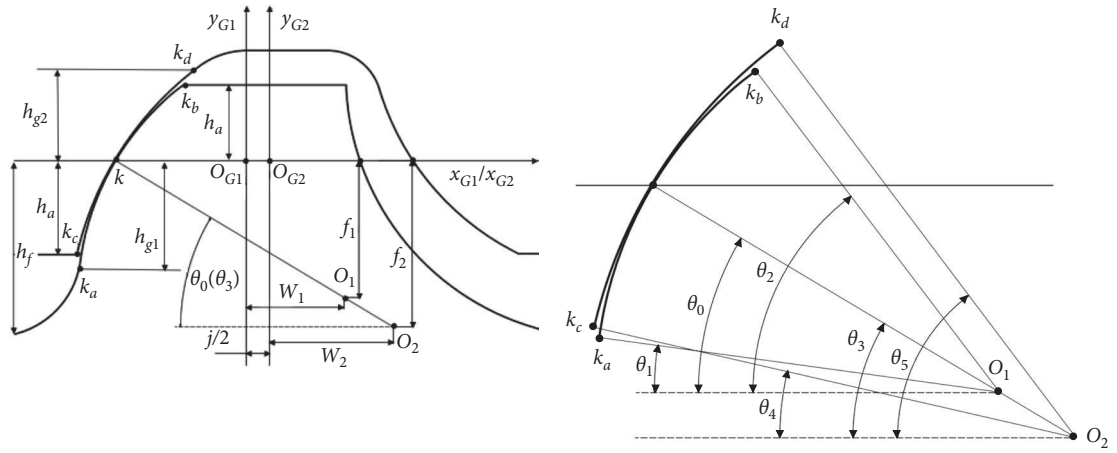

(a) (b)

Figure 8: Meshing profiles of the asymmetric logarithmic spiral gear.

Table 1: Calculation formulas of the tooth profile parameters.

Parameter	Computational formula
Process angle of convex tooth profile θ_1	$\theta_1 = \arcsin\left(r_1 e^{t\times\theta_0}\sin\theta_0 - h_{g1}\right)/r_1 e^{t\times\theta_0}$
Terminal angle of convex profile θ_2	$\theta_2 = \arcsin\left(h_a + f_1\right)/r_1 e^{t\times\theta_2}$
Process angle of concave profile θ_4	$\theta_4 = \arcsin\left(r_2 e^{t\times\theta_3}\sin\theta_3 - h_a\right)/r_2 e^{t\times\theta_4}$
Terminal angle of concave profile θ_5	$\theta_5 = \arcsin\left(h_{g2} + f_2\right)/r_2 e^{t\times\theta_5}$
Gear tooth thickness s	$s = 2\left(r_1 e^{t\times\theta_0}\cos\theta_0 - w_1\right)$
Space width e	$e = s + j$
Arc radius at the bottom of convex tooth profile r_{g1}	$r_{g1} = r_1 e^{t\times\theta_1}\sin\theta_1 + h_f - f_1$
Arc radius at the bottom of concave tooth profile r_{g2}	$r_{g2} = \left(h_f - r_2 e^{t\times\theta_5}\sin\theta_5 + f_2\right)/(1-\cos(\pi/2-\theta_5))$

Table 2: The logarithmic helical parameters range.

Parameter	Computational formula
Minimum initial circle radius of the concave profile $r_{2\,\min}$	$r_{2\,\min} = h_a/e^{t\times\theta_3}\sin\theta_3$
Maximum initial circle radius of the concave profile $r_{2\,\max}$	$r_{2\,\max} = 0.645m_n/(e^{t\times\theta_4}\cos\theta_4 - e^{t\times\theta_3}\cos\theta_3)$
Minimum initial circle radius of the convex profile $r_{1\,\min}$	$r_{1\,\min} = (f_2 - r_2 e^{t\times\theta_4}\sin\theta_4)/e^{t\times\theta_0}\sin\theta_0$
Maximum initial circle radius of the convex profile $r_{1\,\max}$	$r_{1\,\max} = 0.895m_n/(e^{t\times\theta_2}\cos\theta_2 - e^{t\times\theta_0}\cos\theta_0)$

respectively. θ_2 and θ_5 are the terminal angles of the convex and concave tooth profiles, respectively.

According to the geometric relationship, the calculation formulas of the tooth profile parameters are shown in Table 1.

The parameters r_1, r_2, and t of the logarithmic helical can be selected in an infinite number of ways, which lead to the uncertainty of the angles θ_1 and θ_5. So, it is important to determine the logarithmic helical parameters. According to the design principle of gear tooth profile [24], the logarithmic helical parameter ranges can be calculated as in Table 2.

2.4. Sliding Ratio. It is assumed that the initial contact points of the tooth surfaces Σ_1 and Σ_2 are K_1 and K_2, respectively, as shown in Figure 9. After m time, the tooth surfaces Σ_1 and Σ_2 are tangent at K. The arc length of the contact point passing through the tooth surface Σ_1 is S_1. The arc length of the contact point K passing through the tooth surface Σ_2 is S_2.

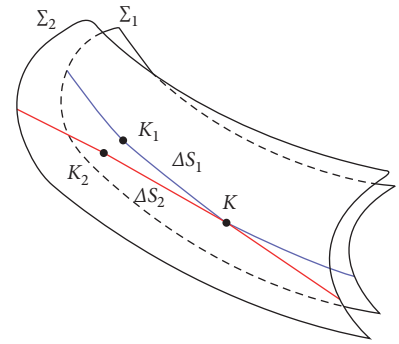

Figure 9: Slide diagram of tooth surfaces [20].

Then, the slip rates of the tooth surfaces Σ_1 and Σ_2 can be calculated, respectively, as follows:

$$\eta_1 = \lim_{\Delta S_1 \to 0} \frac{\Delta S_1 - \Delta S_2}{\Delta S_1} = \frac{\dfrac{dS_1}{dm} - \dfrac{dS_2}{dm}}{\dfrac{dS_1}{dm}} = \frac{dS_1 - dS_2}{dS_1}. \tag{16}$$

$$\eta_2 = \lim_{\Delta S_2 \to 0} \frac{\Delta S_2 - \Delta S_1}{\Delta S_2} = \frac{\dfrac{dS_2}{dm} - \dfrac{dS_1}{dm}}{\dfrac{dS_2}{dm}} = \frac{dS_2 - dS_1}{dS_2}, \tag{17}$$

where $dS_1 = \sqrt{dx_1^2 + dy_1^2 + dz_1^2}dm$, $dS_2 = \sqrt{dx_2^2 + dy_2^2 + dz_2^2}dm$.

The values of the gear slip rate can be obtained from the tooth surface working line equations [20]. Then, Equations (18) and (19) can be obtained by Equations (13) and (14).

$$dS_1 = \sqrt{(a_0 - f_1 + R_1)^2 + \left(\frac{(a_0 - f_1)(ta_0 + b_0)\cos\beta}{tb_0 - a_0}\right)^2 + (R_1 \cot\beta)^2} \cdot \omega_1 dm. \tag{18}$$

$$dS_2 = \sqrt{(a_3 - f_2 - R_2)^2 + \left(\frac{(a_3 - f_2)(ta_3 + b_3)\cos\beta}{tb_2 - a_2}\right)^2 + (R_2 \cot\beta)^2} \cdot \omega_2 dm. \tag{19}$$

By combining Equations (18) and (19) with Equation (15), $dS_1 = dS_2$ can be obtained. The sliding rates of the two meshing teeth surfaces are zero, which verify the gear pure rolling contact.

3. Interference Analysis

When designing an asymmetric logarithmic spiral gear, it is easy to interfere if the tooth profile parameters are determined without rules. Although it is possible to establish the gear model to distinguish the gear without interference, a great deal of work will be done in this way. Therefore, the geometric interference and root cutting conditions of the gear are derived to obtain the allowed range of θ_1 and θ_5. Then, the overlapping interference of the end face profile is examined.

3.1. Geometric Interference of Tooth Profile. As shown in Figure 8, when the concave and convex tooth profiles are meshing, for avoiding geometric interference, h_{g1} and h_{g2} should be greater than h_a. The equations of the geometric interference condition are derived.

$$\begin{aligned} r_2 e^{t \times \theta_5} \times \sin\theta_5 - f_2 > r_1 e^{t \times \theta_2} \times \sin\theta_2 - f_1, \\ f_1 - r_1 e^{t \times \theta_1} \sin\theta_1 > f_2 - r_2 e^{t \times \theta_4} \sin\theta_4. \end{aligned} \tag{20}$$

In the gear design process, when the basic parameters h_a, h_f, r_1, r_2, t, θ_0, and θ_3 are given in Table 1, the angles θ_2 and θ_4 can be solved. By Equation (20), the ranges of the angles θ_1 and θ_5 without geometric interference are calculated.

3.2. Root Cutting. The tangent direction of any point K on the surface along any curve L on the surface is expressed as $dr_k/dm = \partial r_u/\partial u\ (du/dm) + \partial r_v/\partial v\ (\partial v/dm)$, as shown in Figure 10. If the guide vector is zero, the conditional formula of the singular point is established. The boundary equations of gear root cutting are obtained by excluding the singular points on the tooth surface.

The following boundary equations can be derived by referring to the root cutting conditions of the circular arc gear [23]:

$$\cos\theta_{ix} = 0 \quad (x = 1, 2). \tag{21}$$

$$\begin{pmatrix} \sin^4\theta_{ix} + \left(\dfrac{R_x}{r_x e^{t \times \theta_i} \sin^2\beta} - \dfrac{f_x}{r_x e^{t \times \theta_i}}\right) \sin^3\theta_{ix} \\ -\dfrac{f_x^2}{(r_x e^{t \times \theta_{ix}})^2} \cot^2\beta + \dfrac{f_x}{r_x e^{t \times \theta_{ix}}} \cot^2\beta \sin\theta_{ix} \end{pmatrix} = 0 \quad (x = 1, 2), \tag{22}$$

where the subscript $x(1, 2)$ in the formulas represents the convex and concave tooth profiles of the asymmetric logarithmic spiral gear. Aiming at the concave surface, θ_{i2} should be replaced by $-\theta_{i2}$.

The solution of Equation (22) can be obtained by Newton iteration [23].

3.3. Profile Overlapping Interference. As shown in Figure 11(a), the coordinate system $S_g(O_1\text{-}x_g y_g)$ is setup. The gear 1 center point O_1 is taken as the origin of the coordinate system $S_g(O_1\text{-}x_g y_g)$. x_g axis coincides with the centerline of the end face tooth thickness of tooth a. y_g axis is perpendicular to x_g axis. It is assumed that the gear 1 is fixed and the gear 2 rotates counterclockwise around the gear 1. According to the principle of gear relative motion, the tooth b endpoint A_{B1} encloses curve σ_1. If this curve σ_1 intrudes into the tooth of a convex tooth profile, the interference will occur. As shown in

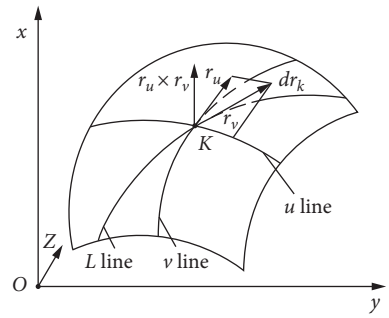

FIGURE 10: The guide vector of the surface.

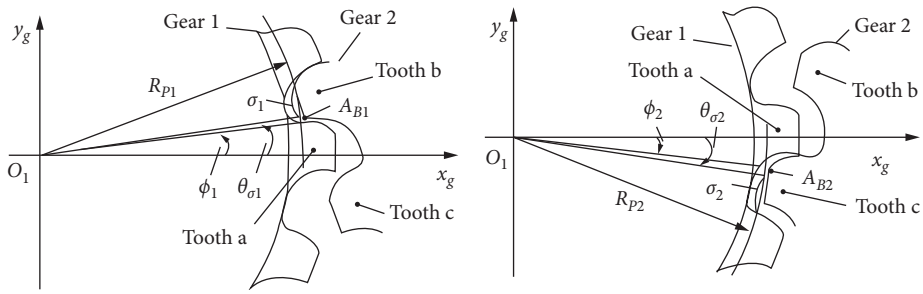

FIGURE 11: Interference diagram of the tooth profile end points.

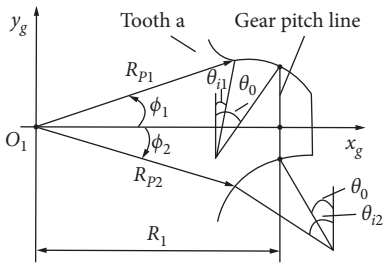

FIGURE 12: Schematic diagram of polar coordinates of tooth a.

Figure 12, it is assumed that the polar coordinate of any point on the convex tooth profile of tooth a is (R_{P1}, Φ_1). The polar coordinate of any point on the curve σ_1 with the same radius is (R_{P1}, $\theta_{\sigma 1}$). If $\theta_{\sigma 1} < \Phi_1$. profile overlapping interference occurs.

Figure 11(b) shows the clockwise rotation of the gear 2 around the gear 1. When Figure 11(b) is compared with Figure 11(a), the subscript of the parameters changes from 1 to 2. Similarly, if $\theta_{\sigma 2} < \Phi_2$, profile overlapping interference occurs.

3.3.1. Polar Coordinate Equation of the Tooth a Profiles of the Gear 1 on the End Face. The equations for y_{s1} in Equations (1) and (8) are divided by $\cos\beta$, then Equations (1) and (8) become the end face tooth profile equations. The polar coordinate expressions of the convex and concave tooth profiles of tooth a on the end face can be obtained as follows:

$$\varphi_x = \arctan \frac{\pm(r_x e^{t\theta_{ix}} \cdot \cos\theta_{ix} - r_x e^{t\theta_0} \cdot \cos\theta_0) + s_1/2}{(R_1 + r_x e^{t\theta_{ix}} \cdot \sin\theta_{ix} - r_x e^{t\theta_0} \cdot \sin\theta_0) \cdot \cos\beta} \quad (x = 1, 2). \tag{23}$$

$$R_{Px} = \frac{\pm(r_x e^{t\theta_{ix}} \cdot \cos\theta_{ix} - r_x e^{t\theta_0} \cdot \cos\theta_0) + s_1/2}{\sin\varphi_x \cdot \cos\beta} \quad (x = 1, 2), \tag{24}$$

where the subscript x(1, 2) in the formula represents the convex and concave tooth profiles. When $x = 1$, the sign is positive and when $x = 2$, the sign is negative.

3.3.2. Polar Coordinate Equations of the Curves σ_1 and σ_2. As shown in Figure 13, X_1 coincides with the centerline of the end face tooth thickness of tooth a and X_2 coincides with the centerline of the end face tooth thickness of tooth b. The position of the centerlines X_1 and X_2 is denoted by the angles δ_1 and δ_2, respectively. Figure 13(a) shows the state of the gear 2 rotating counterclockwise. Figure 13(b) shows the state of the gear 2 rotating clockwise.

According to the law of sine and cosine and the gear meshing principle [25], the gear angular position relation can be known. Then, $\theta_{\sigma 1}$ and $\theta_{\sigma 2}$ can be expressed as follows:

$$\theta_{\sigma x} = \begin{pmatrix} \arcsin \dfrac{\sqrt{4a^2 R_{\mathrm{Bx}}^2 - (a^2 + R_{\mathrm{Bx}}^2 - R_{\mathrm{Px}}^2)^2}}{2aR_{\mathrm{Px}}} + \\ \dfrac{z_2}{z_1} \cdot \left(\arccos \dfrac{a^2 + R_{\mathrm{Bx}}^2 - R_{\mathrm{Px}}^2}{2aR_{\mathrm{Bx}}} - \theta_{\mathrm{Bx}} \right) + \dfrac{(s_1 + s_2)}{m_{\mathrm{n}} z_1} \end{pmatrix} \quad (x = 1, 2), \tag{25}$$

where a is the center distance of the gear pair. The parameters R_{B1}, R_{B2}, θ_{B1}, and θ_{B2} can be known from the geometry of the gear 2, as shown in Figure 14.

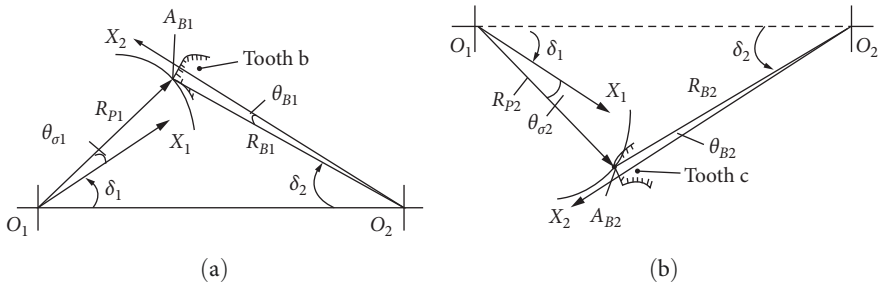

Figure 13: Relative position of the tooth profiles during the gear transmission.

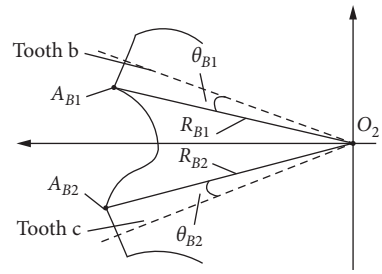

Figure 14: Geometric parameters of gear 2.

Table 3: Basic parameters of the asymmetric logarithmic spiral gear.

Parameter	Value	Parameter	Value
Number of teeth z_1/z_2	42/42	Gear tooth thickness s (mm)	4.62
Normal module m_n (mm)	3	Space width e (mm)	4.8
Tooth width b (mm)	44	Standard pitch diameter d (mm)	133.0008
Spiral angle β (°)	18.67	Tip diameter d_a (mm)	135.4008
Pressure angle θ_0/θ_3 (°)	24	Root diameter d_f (mm)	129.4008
Center distance a (mm)	133.0008	Tooth addendum h_a (mm)	1.2
Side clearance j (mm)	0.18	Tooth dedendum h_f (mm)	1.8

4. Modeling and Stress Analysis

4.1. Basic Parameters. The basic parameters of the asymmetric logarithmic spiral gear are shown in Table 3.

To avoid interference, the logarithmic helical coefficient should be less than zero. So, choose the logarithmic helical coefficient of −0.0025. By substituting the known parameters into the calculation formulas in Table 2, the value ranges of the parameters r_1 and r_2 can be calculated. Referring to the pure rolling single arc gear [16], $r_1 = 1.4\ m_n$ is selected. In order to reduce the tooth surface contact stress, the difference between r_1 and r_2 should be kept as small as possible without interference. Using the method of judging the profile overlapping interference, $r_2 = 2r_1$ is selected. The other parameters of the tooth profiles can be obtained by Table 1 and Equation (15). θ_1 and θ_5 are still unknown. Therefore, the tooth profile parameters are selected as described in Table 4.

4.2. Determination of Unknown Parameters. According to Equations (20)–(22), the ranges of the angles θ_1 and θ_5 without geometric interference and root cutting can be obtained, as shown in Table 5.

In Table 5, $\theta_1 = 5°$ and $\theta_5 = 37°$ are chosen for modeling and interference analysis.

The above parameters are substituted into Equations (23)–(25). Then, the change of the angles $\theta_{\sigma1}$ and Φ_1 with the convex tooth profile angle are plotted, as shown in Figure 15(a). The change of the angles $\theta_{\sigma2}$ and Φ_2 with the concave tooth profile angle are plotted, as shown in Figure 15(b). It is known that the angles $\theta_{\sigma1}$ and $\theta_{\sigma2}$ are greater than the angles Φ_1 and Φ_2, respectively. Thus, the tooth profiles on the end face of the gears do not interfere.

4.3. Establishment of the Gear Models. The single-tooth model is obtained by sweeping the tooth profiles of both end faces along the helical lines, as shown in Figures 16(a) and 16(b). The complete gear model can be established by array method.

4.3.1. Verification of the Noninterference Model. Several meshing teeth are selected for interference detection under 100 Nm load. As can be seen from Figure 17, there are two contact points between the two gears and no interference occurs elsewhere. Therefore, the above selected gear parameters meet the requirements.

Table 4: The parameters of the logarithmic spiral tooth profile.

Parameter	Numerical value of convex tooth profile	Numerical value of concave tooth profile
Convex and concave tooth profile initial circle radius r_1/r_2 (mm)	4.2	8.4
Logarithmic screw coefficient t	-2.5×10^{-3}	-2.5×10^{-3}
Convex and concave tooth profile process angle θ_1/θ_4 (°)	–	14.4189
Convex and concave profile termination angle θ_2/θ_5 (°)	49.1265	–
Lateral offset of logarithmic spiral tooth profile center w_1/w_2 (mm)	1.3034	4.8269
Longitudinal offset of logarithmic spiral tooth profile center f_1/f_2 (mm)	1.6088	3.2176

Table 5: The ranges of the angles θ_1 and θ_5.

Parameter	Angle range
Process angle convex tooth profile θ_1 (°)	(0, 5.6657)
End angle of concave profile θ_5 (°)	(35.0327, 41.5016)

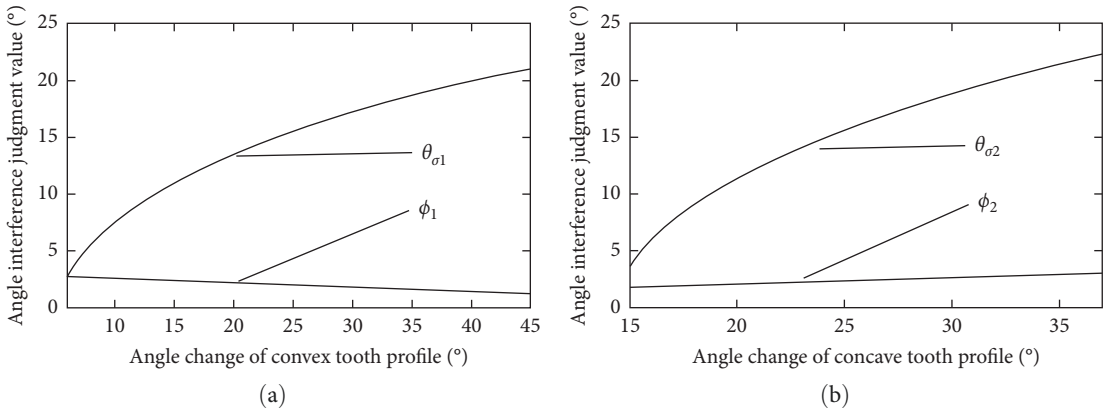

Figure 15: Judgment of the end face tooth profile interference.

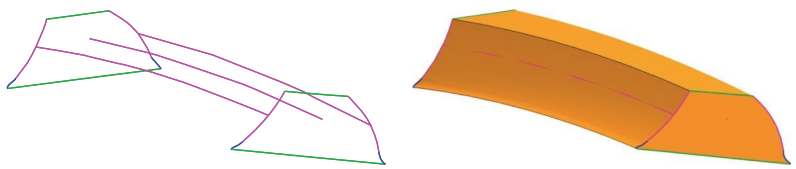

Figure 16: Single tooth formation process of the asymmetric logarithmic spiral gear.

4.3.2. Verification of the Pure Rolling Meshing. As shown in Figure 18, several meshing teeth are selected to verify the pure rolling meshing without load. The tooth surface working lines and contact lines are generated according to Equations (11)–(14). It can be obtained from the measurement command that $\Delta S_1 = \Delta S_2 = 45.8143$ mm, so the gears sliding rates of two meshing surfaces are both zero according to Equations (16) and (17). Therefore, the gear belongs to pure rolling meshing.

4.4. Simulation Stress Analysis

4.4.1. Simulation Setup. The models established above are imported into the finite element software. In grid division, hexahedral grid is adopted, the grid of the gears is set as

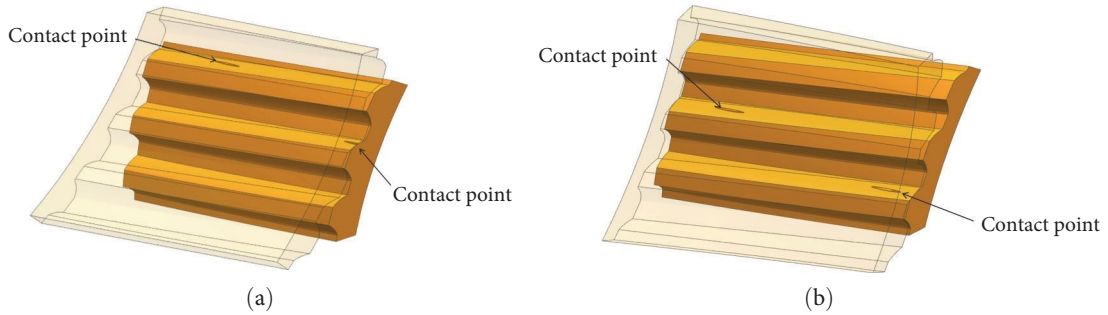

Figure 17: The gears at different turning angles under load: (a) 0°; (b) 10°.

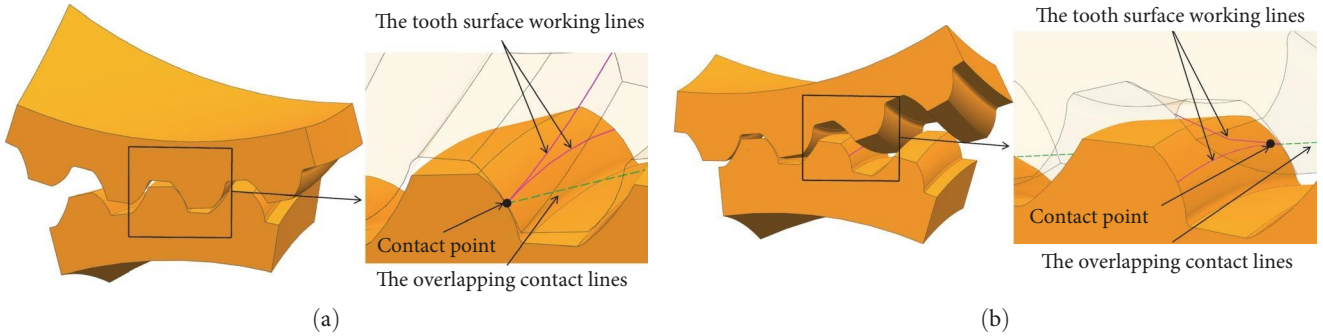

Figure 18: The gears at different turning angles without load: (a) 0°; (b) 10°.

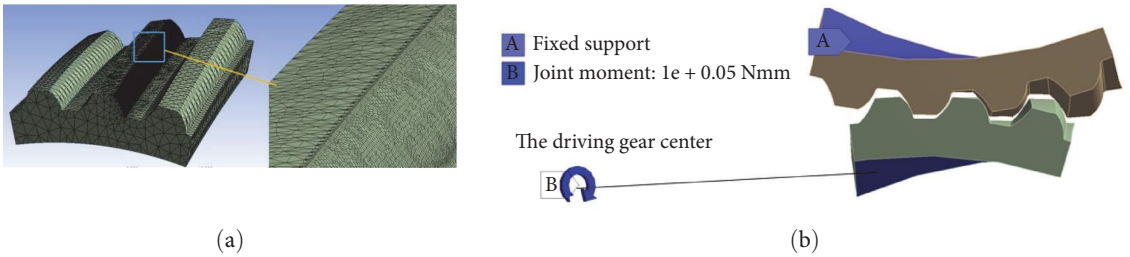

Figure 19: The finite element setting of the asymmetric logarithmic spiral gear.

1 mm, and the grid of the contact teeth surfaces is separately encrypted, as shown in Figure 19(a). In load application, torque is applied to the driving gear. The driven gear is fixed, as shown in Figure 19(b). The material of the gear is steel with Young's modulus $E = 2.09 \times 10^5$ MPa and Poisson's ratio $\mu = 0.3$. The input torque is set as 100 Nm.

The grid of the contact teeth surfaces is separately encrypted as 0.4, 0.3, 0.2, and 0.1 mm. The corresponding maximum contact stresses are obtained by simulation, as shown in Table 6.

As can be seen from Table 6, when the grid of the contact teeth surfaces changes from 0.15 to 0.1 mm, the maximum contact stresses of the teeth surfaces change from 763.02 to 763.11 MPa, and the change rate of the maximum contact stress is 0.09%. Therefore, the grid of the contact teeth surfaces is separately encrypted as 0.15 mm.

4.4.2. Contact Stress. The pure rolling single arc gears with the same size as the asymmetric logarithmic spiral gears are selected and the same simulation parameters are chosen. Then, the gears stress distributions at the tooth width center are obtained, as shown in Figure 20.

Table 6: The grid of the contact teeth surfaces and corresponding maximum contact stresses.

The grid of the contact teeth surfaces (mm)	The maximum contact stress value (MPa)
0.4	577.37
0.3	749.85
0.2	760.33
0.15	762.43
0.1	763.11

As can be seen from Figure 20, the maximum contact stress of the asymmetric logarithmic spiral gear is 757.28 MPa, which occurs on the driven gear. The maximum

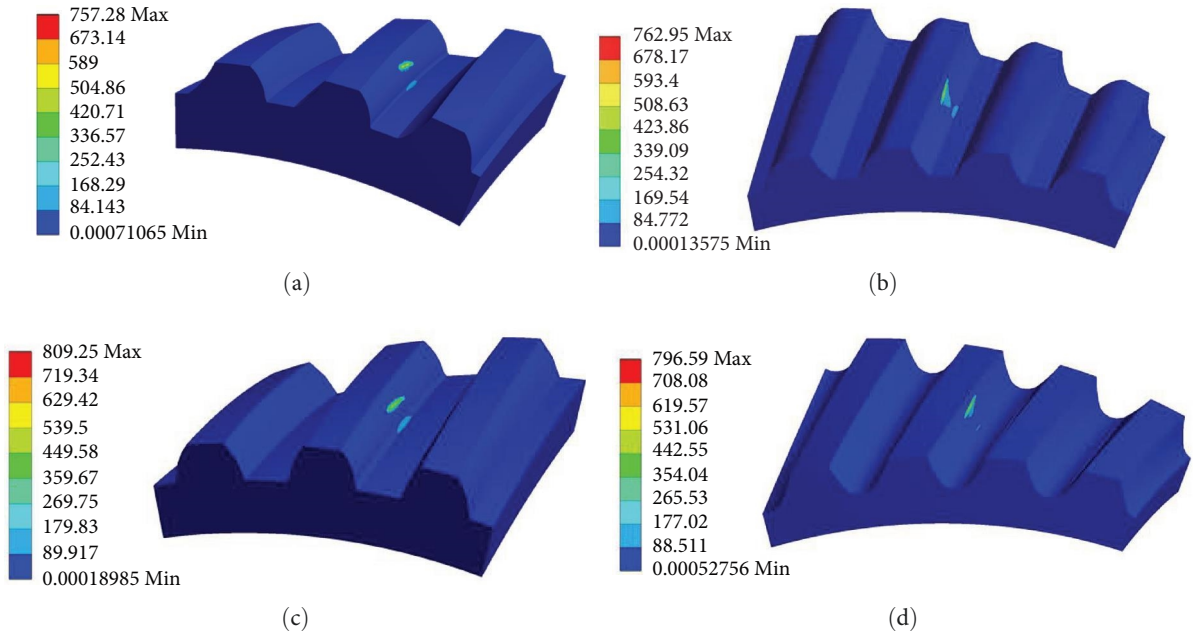

Figure 20: Contact stress: (a) and (b) are the driving and driven gears of the asymmetric logarithmic spiral gear, respectively; (c) and (d) are the driving and driven gears of the pure rolling single arc gear, respectively.

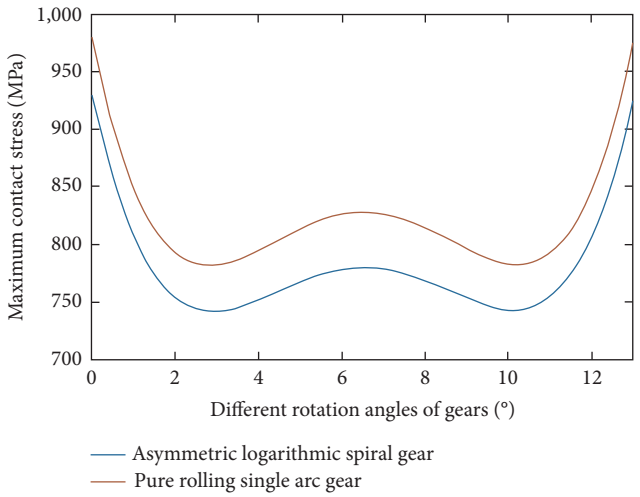

Figure 21: Change of the maximum contact stress at different angles of the gears.

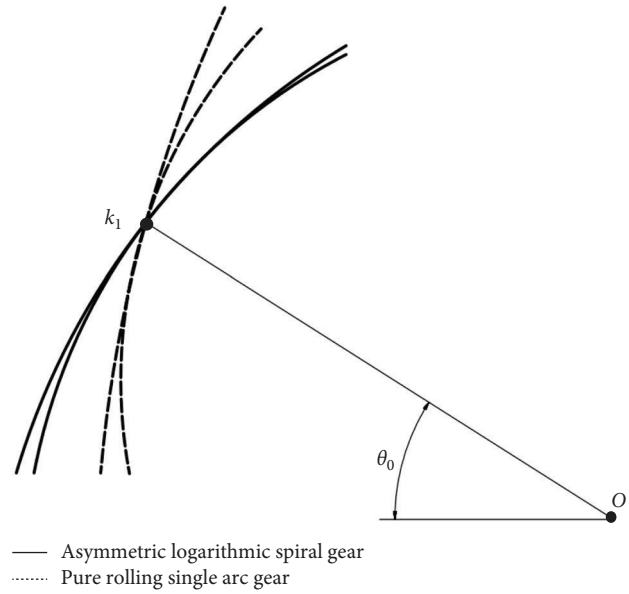

Figure 22: Comparison of the gears tooth shape.

contact stress of the pure rolling single arc gear is 809.25 MPa, which occurs on the driving gear.

In order to understand the change of the maximum contact stress during the gears rotation, finite element analysis is carried out on some positions of the gears rotation. The image drawn from the results is shown in Figure 21.

It can be seen from Figure 21 that the maximum contact stress of the asymmetric logarithmic spiral gear is lower than that of the pure rolling single arc gear. When the rotation angle is zero, the gear contacts at the end face, and the maximum contact stress is larger than that of the other rotation angles of the gears.

As shown in Figure 22, the teeth profiles slope of the asymmetric logarithmic spiral gears contact point k_1 are smaller than that of the pure rolling single arc gears at the same pressure angle θ_0. On the premise of noninterference, the difference of the meshing teeth profiles curvature radius of the asymmetric logarithmic spiral gears is smaller, so the maximum contact stress of the asymmetric logarithmic spiral gear is lower than that of the pure rolling single arc gear.

4.4.3. Bending Stress. The bending stresses of these two gears are extracted by path selection when the gears contact at the center of tooth width, as shown in Figure 23.

As can be seen from Figure 23, the maximum bending stress of the asymmetric logarithmic spiral gear is 162.82 MPa and that of the pure rolling single arc gear is 169.88 MPa. The

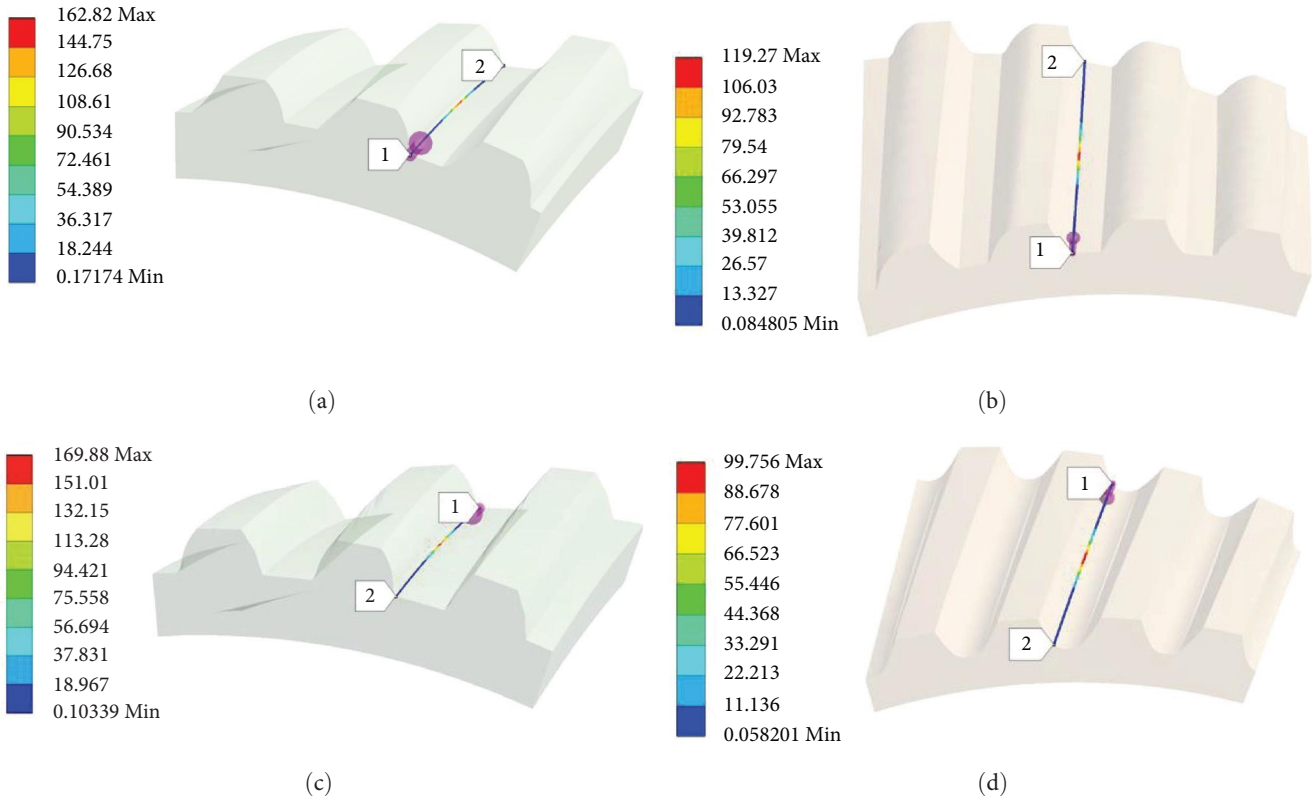

FIGURE 23: Bending stress: (a) and (b) are the driving and driven gears of the asymmetric logarithmic spiral gear, respectively; (c) and (d) are the driving and driven gears of the pure rolling single arc gear, respectively.

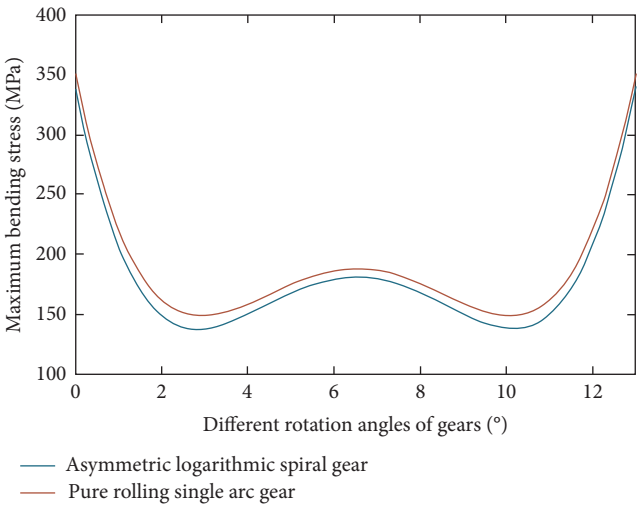

FIGURE 24: Change of the maximum bending stress at different angles of the gears.

maximum bending stress of these two gears occurs on the driving gear.

Similarly, in order to understand the change of the maximum bending stress of the gears rotation, finite element analysis is carried out on some positions of the gears rotation. The image drawn from the results is shown in Figure 24.

It can be seen from Figure 24 that the maximum bending stress of the asymmetric logarithmic spiral gear is lower than that of the pure rolling single arc gear.

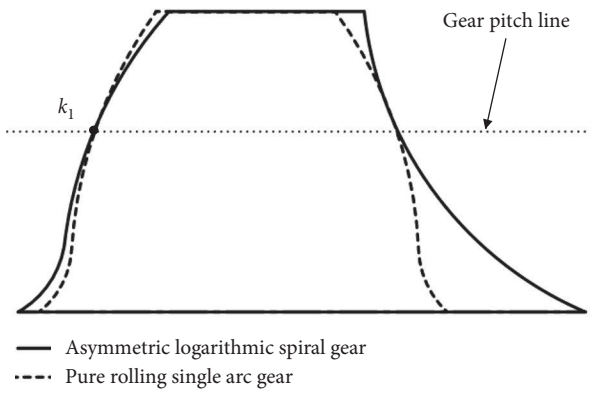

FIGURE 25: Comparison of the gears tooth shape.

As shown in Figure 25, comparing with the pure rolling single arc gear, the root thickness of the asymmetric logarithmic spiral gear increases, so the maximum bending stress is lower than that of the pure rolling single arc gear.

In summary, the asymmetric logarithmic spiral gear shows lower maximum contact and bending stresses than that of the pure rolling single arc gear.

5. Conclusions

In this paper, a new type of pure rolling gear, named as an asymmetric logarithmic spiral gear, is proposed by referring to the tooth shape of the *Issus* planthopper gear. The main conclusions of this paper can be drawn as follows:

(1) To explore the meshing principle of this kind of gear, the equations of the tooth surfaces, working line, and contact line are derived. The conditions of the pure rolling gear are determined. The calculation formulas of the tooth profile parameters and slip rates are obtained. The results show that the slip rates of the meshing teeth surfaces are zero, which verify that it is a kind of pure rolling gear in theory.

(2) To ensure accurate gear engagement, the geometric interference, root cutting, and tooth profile interference are analyzed theoretically. The appropriate parameters are selected to establish three-dimensional solid models to simulate the gear transmission process. The results show that the noninterference gear pair can be successfully designed using the proposed method.

(3) The stress distributions of the asymmetric logarithmic spiral gear and pure rolling single arc gear are analyzed by finite element method. The results show that the asymmetric logarithmic spiral gear has lower contact stress and bending stress than the pure rolling single arc gear. Furthermore, the asymmetric logarithmic spiral gear can be machined only with one tool. So, the performance and manufacturability of the asymmetric logarithmic spiral gear are better than that of the pure rolling single arc gear.

The related investigations on this novel type of gear pair, which include: (1) tooth profile modification considering deformation and error; (2) fatigue life of the gear; and (3) processing and prototype performance test of the gear, are being carried out or would be the next step of work by the authors. Efforts putting this drive forward into practical application are also needed in the near future.

Data Availability

Data can be obtained from Zenghuang He upon request.

Conflicts of Interest

The authors declare that they have no conflicts of interest.

Authors' Contributions

Zenghuang He carried out the construction of the model logic and writing. Xu Gong build model derivation and simulation model. Shengping Fu checked the model and revised the paper. Shanming Luo proposed ideal and thesis revision. Jingyu Mo respond to thesis revisions.

Acknowledgments

This work was partially supported by the National Natural Science Foundation of China (grant nos. 51405410, 52205055, and 51975499) and the Natural Science Foundation of Fujian Province, China (grant no. 2019J01862). The authors would like to express gratitude to their financial support.

References

[1] R. Tan, B. Chen, and C. Peng, "General mathematical model of spiral bevel gears of continuous pure-rolling contact," *Proceedings of the Institution of Mechanical Engineers, Part C: Journal of Mechanical Engineering Science*, vol. 229, no. 15, pp. 2810–2826, 2015.

[2] Z. Chen, M. Zeng, and A. Fuentes-Aznar, "Computerized design, simulation of meshing and stress analysis of pure rolling cylindrical helical gear drives with variable helix angle," *Mechanism and Machine Theory*, vol. 153, Article ID 103962, 2020.

[3] Z. Chen, M. Zeng, and A. Fuentes-Aznar, "Geometric design, meshing simulation, and stress analysis of pure rolling cylindrical helical gear drives," *Proceedings of the Institution of Mechanical Engineers, Part C: Journal of Mechanical Engineering Science*, vol. 234, no. 15, pp. 3102–3115, 2020.

[4] Z. Chen and M. Zeng, "Design of pure rolling line gear mechanisms for arbitrary intersecting shafts," *Proceedings of the Institution of Mechanical Engineers, Part C: Journal of Mechanical Engineering Science*, vol. 233, no. 15, pp. 5515–5531, 2019.

[5] X. Xiao, Y. Chen, X. Xie, and Y. Shao, "A miniature noncircular line gear with pure-rolling contact," *Journal of Advanced Mechanical Design, Systems, and Manufacturing*, vol. 15, no. 6, Article ID JAMDSM0071, 2021.

[6] C. He, Y. Chen, W. Lin, and Y. Lyu, "Research on the centre distance separability of parallel shaft line gear pair," *Proceedings of the Institution of Mechanical Engineers, Part C: Journal of Mechanical Engineering Science*, vol. 236, no. 6, pp. 3261–3274, 2022.

[7] M. J. Wagner, W. F. Ng, and S. G. Dhande, "Profile synthesis and kinematic analysis of pure rolling contact gears," *Journal of Mechanical Design*, vol. 114, no. 2, pp. 326–333, 1992.

[8] X. H. Tao, H. H. Wang, J. S. Chen, J. X. Yang, and X. J. Wang, "Geometrical feature analysis of the movement of the new type of double-hemisphere rolling gear globoidal cam indexing mechanism," *Advanced Materials Research*, vol. 706–708, pp. 1379–1384, 2013.

[9] Y. Song, Q. Liao, S. Wei, and L. Guo, "Research on pure rolling cycloid-like reducers used in industrial robot," in *2014 IEEE International Conference on Information and Automation (ICIA)*, pp. 305–310, IEEE, Hailar, China, 2014.

[10] Y. N. Xue, Y. Wang, and Z. Wang, "Meshing theory of new epicycloids gear drive," *Advanced Materials Research*, vol. 383-390, pp. 5238–5241, 2011.

[11] R. Tan, B. Chen, D. Xiang, and D. Liang, "A study on the design and performance of epicycloid bevels of pure-rolling contact," *Journal of Mechanical Design*, vol. 140, no. 4, Article ID 043301, 2018.

[12] X. P. Huang and A. P. Huang, "Principle and realization of pure rolling contact gearing," *Mechanical Transmission*, vol. 3, pp. 5–8, 2001.

[13] Z. Chen, H. Ding, B. Li, L. Luo, L. Zhang, and J. Yang, "Geometry and parameter design of novel circular arc helical gears for parallel-axis transmission," *Advances in Mechanical Engineering*, vol. 9, no. 2, 2017.

[14] Y. L. Geng, *Theoretical Analysis and Motion Simulation of Pure Rolling Single Arc Gear*, Nanjing Forestry University, 2010.

[15] C. M. Zhou, *Measuring Theory of Pure Rolling Contact Gear*, Nanjing Forestry University, 2010.

[16] L. L. Zhao, *Study on Parametric Design and Mechanical Properties of Pure Rolling Single Arc Gear*, Nanjing Forestry University, 2019.

[17] D. Liang, B. Chen, Y. Gao, S. Peng, and S. Qin, "Geometric and meshing properties of conjugate curves for gear transmission," *Mathematical Problems in Engineering*, vol. 2014, Article ID 484802, 12 pages, 2014.
[18] D. Liang, B. Chen, Y. Gao, and Y. Zhang, "Generation principle and meshing characteristics of conjugate-curve circular arc gears," *Journal of Advanced Mechanical Design, Systems, and Manufacturing*, vol. 9, no. 1, Article ID JAMDSM0005, 2015.
[19] D. Liang, B. K. Chen, and Y. E. Gao, "Calculation method of sliding ratios for conjugate-curve gear pair and its application," *Journal of Central South University*, vol. 22, pp. 946–955, 2015.
[20] D. Liang, *Research on Meshing Theory of Conjugate-Curve Gear Transmission*, Chongqing University, 2015.
[21] M. Burrows and G. Sutton, "Interacting gears synchronize propulsive leg movements in a jumping insect," *Science*, vol. 341, no. 6151, pp. 1254–1256, 2013.
[22] G. P. Wang, *Study on Gearing Theory of Logarithmic Spiral Bevel Gear*, Inner Mongolia University of Technology, 2007.
[23] X. Z. L. Xianzan and J. K. Shang, *Meshing Principle of Arc Gear*, pp. 56–61, Mechanical Industry Press, 2003.
[24] X. L. Zhu, *Handbook of Gear Design*, Chemical Industry Press, 2010.
[25] H. Sun, *Mechanical Principle*, Higher Education Press, 2000.